INORGANIC CHEMISTRY FRONTIERS

RESEARCH ARTICLE

View Article Online
View Journal | View Issue

Cite this: *Inorg. Chem. Front.*, 2025, **12**, 1927

Dual-band white light emission and temperature-dependent luminescence of Sn^{2+} in the metastable structure of $Cs_2CaCl_4(H_2O)_2$†

Hu Wang,[a] Yuexiao Pan, *[a] Zhenyu Shi,[a] Yeling Cao,[a] Hongzhou Lian,[b] Jun Lin, *[b] Qian Miao[a] and Jun Zou *[c,d]

Received 21st December 2024,
Accepted 13th January 2025

DOI: 10.1039/d4qi03288h

rsc.li/frontiers-inorganic

The quest for novel luminescent materials with tunable color emission and temperature-sensing capabilities remains a vibrant field of research, particularly for applications in solid-state lighting and security features. The as-synthesized rod-like crystal $Cs_2CaCl_4(H_2O)_2$:Sn^{2+} (*R*-CCCH:Sn^{2+}) exhibits dual-band white light emission characterized at 415 nm and 540 nm, which correspond to the singlet state and triplet state transitions of Sn^{2+}, respectively. Upon heating from 298 to 428 K, an anomalous enhancement in the intensity of the 415 nm emission in *R*-CCCH:Sn^{2+} was observed while its 540 nm emission underwent significant thermal quenching. The observation of the temperature-dependent photoluminescence (PL) indicates that *R*-CCCH:Sn^{2+} exists in a metastable state. Upon calcination at 428 K for 20 min, *R*-CCCH:Sn^{2+} changed to the stable state particle-like crystal $Cs_2CaCl_4(H_2O)_2$:Sn^{2+} (*P*-CCCH:Sn^{2+}), exhibiting STEs of the CCCH matrix and the $^3P_1 \rightarrow {}^1S_0$ transition of Sn^{2+}. The significance of this work lies in the discovery of the metastable state in CCCH and the manipulation of Sn^{2+} to emit both singlet and triplet transitions, leading to white light emission.

1 Introduction

The advent of white light-emitting diodes (WLEDs) has revolutionized the lighting industry, offering energy efficiency and environmental sustainability over traditional lighting technologies. The pursuit of phosphors capable of emitting white light from a single-component system has intensified due to their potential to simplify WLED device architecture and enhance color stability.[1–8] In this context, halide perovskites have emerged as promising candidates, exhibiting a combination of high photoluminescence quantum yields (PLQYs), adjustable bandgaps, and facile synthesis methods.[4–8] However, due to their toxicity, traditional perovskite luminescent materials containing lead and cadmium are limited to large-scale applications in the market.[5,9–11] The appeal of environmentally friendly, non-toxic single-component white light emitters is further amplified by their potential to offer a sustainable solution aligned with the growing demand for eco-friendly lighting technologies.

The interplay between the host lattice and dopants has been a subject of extensive research, as evidenced by numerous studies.[12–17] For instance, Mn^{2+} doped halide perovskites exhibit a broad yellow emission that can be tuned to green emission by varying the crystal structure through raising the ambient temperature.[12] Similarly, Sb^{3+} ions in single and double perovskite hosts display distinct emission bands, highlighting the sensitivity of the $^3P_0 \rightarrow {}^1S_0$ transition to the local lattice environment.[13] Despite these advances, our understanding of the structure–property relationships in luminescent materials is still incomplete. A deeper comprehension of these relationships is crucial for the rational design of materials with desired luminescence properties.

The Sn^{2+} doped PL materials have garnered considerable attention due to their distinctive photoluminescence properties.[4,18–25] The luminescence of Sn^{2+} ions is predominantly attributed to their $5s^2$ electronic configuration, which upon excitation can lead to the s–p transition. Particularly, the emission characteristics of Sn^{2+} are highly susceptible to the local coordination environment. For instance, in the Cs_2ZnCl_4:Sn^{2+} system, at 270 K, the observation is limited to a single

[a]*Key Laboratory of Carbon Materials of Zhejiang Province, College of Chemistry and Materials Engineering, Wenzhou University, Wenzhou 325035, P.R. China. E-mail: yxpan@wzu.edu.com*
[b]*State Key Laboratory of Rare Earth Resource Utilization, Changchun Institute of Applied Chemistry, Chinese Academy of Sciences, Changchun 130022, P. R. China. E-mail: jlin@ciac.ac.cn*
[c]*Institute of New Materials & Industrial Technology, Wenzhou University, Wenzhou 325024, China*
[d]*School of Science, Shanghai Institute of Technology, Shanghai, 201418, China. E-mail: zoujun@sit.edu.cn*

†Electronic supplementary information (ESI) available. See DOI: https://doi.org/10.1039/d4qi03288h

emission centered at 648 nm, which is assigned to the $^3P_1$ to $^1S_0$ transition. However, at 30 K, the emission profile diversifies due to the enhanced Jahn–Teller effect, resulting in two distinct emission peaks.[18] Sn^{2+}-doped zero-dimensional Cs_2ZnBr_4 demonstrates a single, broad near-infrared emission band peaking at around 700 nm.[19] Hexagonal phase $CsCdCl_3$ has successfully demonstrated an ultralong (>2000 s) persistent luminescence by incorporating Sn^{2+} ions, achieving the highest recorded PLQY (84.47%) among the current halide perovskites.[20] However, Sn^{2+}-doped 0D Rb_4CdCl_6 with an emission at 485 nm by a simple hydrothermal method only have a near-unity quantum efficiency (PLQY ~98.04%).[21] Thus, a profound comprehension of the luminescence mechanisms of Sn^{2+} in different structures is vital for the development of new high-performance luminescent materials.

In our previous work, we synthesized *P*-CCCH, which emits blue light at 465 nm through STE. Upon doping with Sn^{2+}, an additional emission peak at 490 nm, attributed to Sn^{2+}, was observed, indicating a single emission band.[22] In this work, we increased the amount of hypophosphite used in the synthesis procedure and found not only a change in the morphology from particle to rod-like but also distinct photoluminescence properties. The rod-shaped *R*-CCCH does not emit light inherently, but after Sn^{2+} doping, it exhibits two distinct emission bands. Through decay measurements, we determined these bands to correspond to the singlet and triplet state emissions of Sn^{2+}. Importantly, with an increase in temperature, the singlet state emission intensifies while the triplet state emission diminishes, causing a shift in the luminescence color from yellow to cyan. Furthermore, we observed that the rod-shaped *R*-CCCH irreversibly transforms into particle-shaped *P*-CCCH under annealing. This behavior suggests that the metastable state of *R*-CCCH is highly sensitive to thermal stimuli, offering potential for temperature sensing applications.

2 Experimental

2.1 Synthesis of *R*-CCCH:Sn^{2+} and *P*-CCCH:Sn^{2+}

The synthesis of the rod-shaped crystal *R*-CCCH doped with 3% Sn^{2+} was achieved by introducing 1.94 mmol of $CaCl_2$, 4 mmol of CsCl, and 0.06 mmol of $SnCl_6{\cdot}6H_2O$ into a 15 mL polytetrafluoroethylene lined stainless-steel autoclave. Following this, 3 mL of 37 wt% hydrochloric acid and 600 μL of 50 wt% hypophosphorous acid (H_3PO_2) were added to the mixture to ensure complete dissolution. The autoclave was then sealed and heated at 160 °C for a duration of 12 h in an oven. Post the reaction period, the autoclave was naturally cooled to room temperature, yielding the objective product. To explore the influence of the concentration of H_3PO_2 on the PL properties of CCCH:Sn^{2+}, a series of experiments were conducted with varying volumes of H_3PO_2 (such as 100, 200, 300, 400, 500, 600, and 800 μL), while maintaining all other conditions constant. For the synthesis of particle-shaped *P*-CCCH:Sn^{2+}, which has been previously described, a similar approach was adopted except that the amount of H_3PO_2 was adjusted to 100 μL.[22]

2.2 Characterization

The synthesized *R*-CCCH:Sn^{2+} and *P*-CCCH:Sn^{2+} samples were subjected to comprehensive characterization to assess their morphological, crystallographic, and photoluminescence attributes. X-ray powder diffraction (XRD) measurements were performed on a Bruker D8 Advance diffractometer utilizing Cu K_α radiation (λ = 0.15418 nm). The diffraction patterns were recorded at a scan speed of 10° per minute over a 2θ range from 10° to 50°. For the analysis of the photoluminescence properties, a FluoroMAX-4-TCSPC spectrophotometer, which is equipped with a 450 W xenon lamp and a photomultiplier tube, was used to acquire the photoluminescence excitation (PLE) and emission spectra over a wavelength span of 200 to 900 nm. X-ray photoelectron spectroscopy (XPS) was employed to probe the valence state of tin ions using a Thermo ESCALAB 250 Xi system with a monochromatic Al Kα X-ray source.

2.3 Encapsulation process of *R*-CCCH:Sn^{2+} on LED chips

The *R*-CCCH:Sn^{2+} crystals and K_2SiF_6:Mn^{4+} were crushed into a fine powder and homogeneously blended with a commercial A-grade epoxy resin and a corresponding B-grade curing agent at a mass ratio of 1 : 4 to achieve a consistent particle size distribution throughout the mixture. The mixture was then encapsulated within a 285 nm ultraviolet (UV) transparent chip and subjected to a drying process at 80 °C for a duration of 2 hours to cure the resin and stabilize the phosphor, yielding a warm white light-emitting material.

3 Results and discussion

The synthesis process of Sn^{2+}-doped CCCH-based crystals is depicted in Fig. 1a. It can be clearly observed that when the volume of H_3PO_2 is 100 μL and 600 μL, granular and rod-shaped crystals are obtained, respectively. This indicates that in this reaction system, the addition of more H_3PO_2 not only serves as a reducing agent but also acts as a solvent. A larger volume of solvent (*e.g.*, 600 μL) may facilitate better dissolution of reactants, keeping them in a uniformly dispersed state and promoting preferential growth in specific directions, thus resulting in the formation of rod-shaped crystals. In contrast, a relatively smaller volume of solvent (*e.g.*, 100 μL) may lead to locally high concentrations of reactants, rapid nucleation, and the formation of small particles, promoting the formation of granular crystals.[26,27] When the amount of H_3PO_2 is increased to 800 μL, a solution is obtained without any product. Fig. S1† shows CCCH:Sn^{2+} crystals synthesized under different reaction conditions with varying amounts of H_3PO_2. The rod-shaped *R*-CCCH:Sn^{2+} crystals exhibit a length of up to 1 cm and a radius of approximately 0.1 cm, with a smooth surface, indicating a high degree of crystallinity. When the volume of H_3PO_2 is 300 μL, granular and rod-shaped crystals are obtained together. The granular morphology and photoluminescence

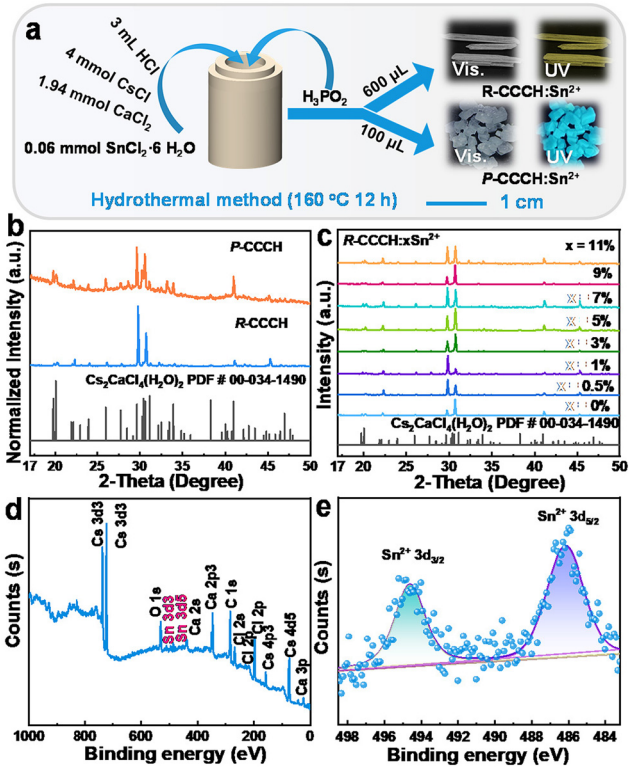

Fig. 1 (a) Fabrication process of *P*/*R*-CCCH:Sn^{2+} samples. Powder XRD patterns of (b) *P*/*R*-CCCH and (c) *R*-CCCH:Sn^{2+} with different doping concentrations. (d) The survey-scan XPS spectrum and (e) $3d_{3/2}$ and $3d_{5/2}$ XPS peaks of Sn^{2+} in *R*-CCCH:Sn^{2+}.

properties of *P*-CCCH:Sn^{2+} have been previously reported in our earlier work.[22] Under 300 nm UV light irradiation, the rod-shaped *R*-CCCH:Sn^{2+} crystals emit yellow light, which is different from cyan light emitted by *P*-CCCH:Sn^{2+}. This difference may be due to the different internal structures of the crystals, which affect the energy level splitting of Sn^{2+} ions in *R*-CCCH and *P*-CCCH crystals.

The XRD patterns displayed in Fig. 1b reveal that the diffraction peaks of both the granular *P*-CCCH:Sn^{2+} and rod-shaped *R*-CCCH:Sn^{2+} crystals match well with those of CCCH (PDF # 00-034-1490), indicating that both samples belong to the pure CCCH phase. The variation in peak intensities observed in the XRD patterns can be attributed to the different orientations resulting from the distinct morphologies of the crystals. In Fig. 1c, the XRD patterns of *R*-CCCH:Sn^{2+} with Sn^{2+} doping concentrations ranging from 0.5% to 11% all show good agreement with the standard card diffraction peaks, suggesting that Sn^{2+} doping merely serves as luminescent centers without altering the crystal structure.

To further confirm the successful doping of Sn^{2+} into the *R*-CCCH crystal, XPS measurements were conducted. The XPS spectrum shown in Fig. 1d indicates the presence of all the expected elemental peaks for Cs 3d, Ca 2p, Cl 2p, Sn 3d, and O 1s in the *R*-CCCH material. Additionally, Fig. 1e presents the high-resolution XPS spectrum of Sn^{2+} 3d in the *R*-CCCH:Sn^{2+} sample, with binding energies of Sn^{2+} $3d_{3/2}$ and Sn^{2+} $3d_{5/2}$ measured at 494.6 eV and 486.2 eV, respectively.[23,25] Moreover, the EDS spectrum in Fig. S2† reveals an element proportion of Cs : Ca : Cl : Sn at 1.6 : 0.8 : 3 : 0.2, which is close to the expected ratio for the *R*-CCCH:3% Sn^{2+} material, further validating the successful incorporation of Sn^{2+} ions.

The PLE spectra of *R*-CCCH:Sn^{2+} presented in Fig. 2a reveal that under monitoring at 540 nm and 415 nm, the intensity of the excitation peaks varies while their positions remain unchanged, indicating that the emissions at 540 nm and 415 nm originate from the same luminescent center. The blue dashed area from 200 to 260 nm corresponds to the $^1S_0$ to $^1P_1$ transition of Sn^{2+}, while the red dashed area from 260 to 340 nm corresponds to the $^1S_0$ to $^3P_2$ and $^3P_1$ transitions. Upon excitation at 284 nm, the emission spectrum of the *R*-CCCH:Sn^{2+} sample spans in the range of 360–700 nm. Gaussian peak fitting of the emission spectrum yields two peaks at 415 nm and 540 nm, which are attributed to the singlet and triplet emissions of Sn^{2+} ions, respectively (Fig. 2b). This is in contrast to the previously reported *P*-CCCH:Sn^{2+}, which emits cyan light with peaks at 465 nm and 492 nm, ascribed to the blue self-trapped emission (STE) from the *P*-CCCH matrix and the triplet transition $^3P_1 \rightarrow {}^1S_0$ of Sn^{2+}.[22] In the current work, the matrix *R*-CCCH does not emit light under UV irradiation; however, upon doping with Sn^{2+}, it exhibits an ultra-wide range of dual-band emissions. This observation suggests that the introduction of Sn^{2+} ions into the *R*-CCCH matrix activates new emission pathways, leading to a broadened and dual-band emission profile.

As shown in Fig. S3–5,† the excitation and emission spectra of *R*-CCCH:xSn^{2+} with varying Sn^{2+} doping concentrations were investigated. The emission peaks of *R*-CCCH:xSn^{2+} intensify with the increase of Sn^{2+} concentration from 0.5% to 5%. A further increase in Sn^{2+} concentration leads to a decrease in luminescence intensity, which is attributed to concentration quenching, with 5% being the optimal doping concentration. Fig. 2c displays the PL spectra and photographs of the crystals under excitation at 250, 270, and 300 nm. It is evident that a decrease in the energy of the excitation wavelength shifts the emission of the *R*-CCCH:Sn^{2+} sample from white to yellow light, due to the varying probabilities of singlet and triplet radiative transitions under different excitations. The Commission Internationale de L'Eclairage (CIE) coordinates (Fig. S6†) shows that the PL of *R*-CCCH:Sn^{2+} under excitation at 250 and 300 nm exhibits white light (0.2982, 0.3645) and yellow light (0.3443, 0.4699), respectively.

Under 284 nm light excitation, the corresponding fluorescence decay curves were characterized to further confirm the assignment of these emission peaks. The PL decay lifetime of the *R*-CCCH:Sn^{2+} sample at 415 nm, as shown in Fig. 2d, decreased from 2.13 ns (1% Sn^{2+}) to 1.45 ns (9% Sn^{2+}) with the increase of Sn^{2+} concentration. Similarly, under 540 nm light monitoring (Fig. 2e), the PL decay lifetime of the *R*-CCCH:Sn^{2+} sample decreased from 29.50 μs (1% Sn^{2+}) to 14.54 μs (9% Sn^{2+}). These lifetimes provide further evidence that the emissions at 415 nm and 540 nm are attributed to the radiative

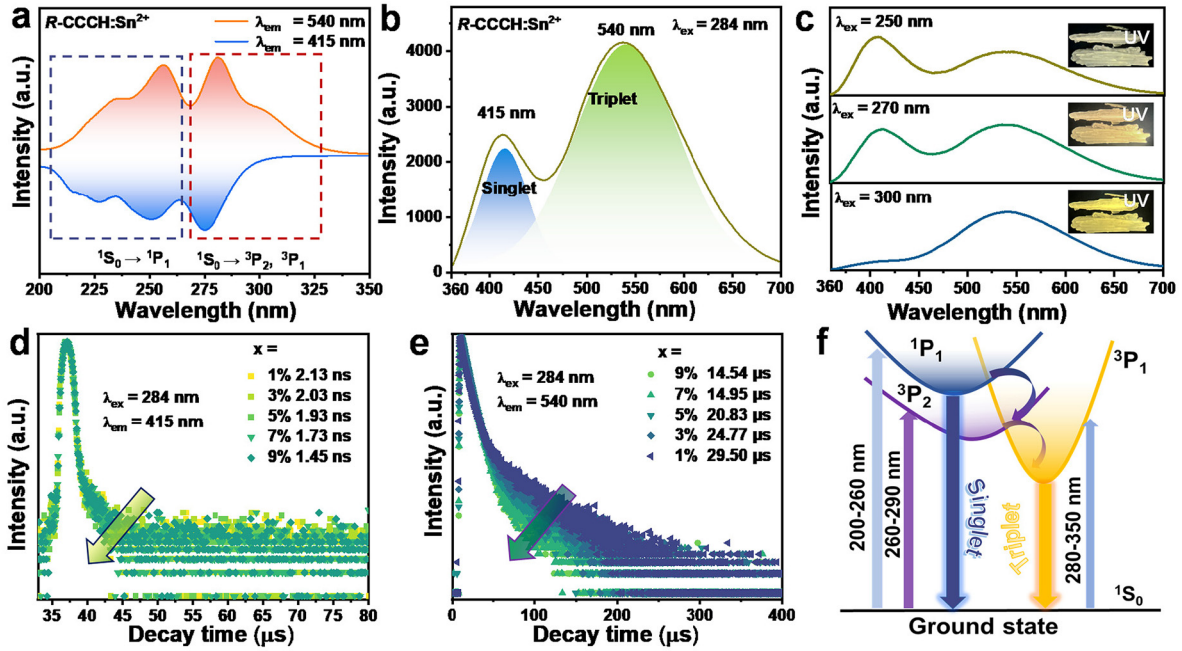

Fig. 2 (a) PLE spectra of *R*-CCCH: Sn^{2+} monitored at different detection wavelengths. (b and c) PL spectra (inset: photographs) of *R*-CCCH:Sn^{2+} excited at different excitation wavelengths. (d and e) PL decay curves *R*-CCCH:*x*Sn^{2+} with various *x* values. (f) Schematic diagram of the PL mechanism involving singlet and triplet self-trapped emission.

transitions from the spin singlet state $^1P_1$ and spin triplet state $^3P_1$ of Sn^{2+} to the ground state $^1S_0$ of Sn^{2+} ions, respectively.[23,28] Moreover, the observed decrease in PL decay lifetime with increasing Sn^{2+} concentration is indicative of concentration quenching effects, which may be due to enhanced energy transfer processes or increased non-radiative recombination pathways.

Based on the above characterization studies, a schematic diagram of the PL mechanism for the *R*-CCCH:Sn^{2+} material was constructed (Fig. 2f). For Sn^{2+} ions with an outer electron configuration of ns^2, the excited state splits into three triplet states ($^3P_0$, $^3P_1$, and $^3P_2$) and one singlet state ($^1P_1$).[11,29,30] Upon UV light excitation, electrons transition from the $^1S_0$ ground state to the singlet state $^1P_1$, and the triplet states $^3P_1$ and $^3P_2$. Subsequently, high-energy electrons undergo non-radiative transitions to both the singlet and triplet states. Ultimately, the electrons return to the $^1S_0$ ground state, resulting in the observed dual-band emission at 415 nm and 540 nm.

The temperature-dependent photoluminescence (PL) spectra of *R*-CCCH:Sn^{2+} and *P*-CCCH:Sn^{2+} materials, as depicted in Fig. 3, provide insights into their thermal stability and emission characteristics. The PL spectra of *R*-CCCH:Sn^{2+}, shown in Fig. 3a, were recorded from 298 K to 428 K under 284 nm excitation. It is observed that the emission peak at 540 nm, attributed to the triplet state, significantly decreases with increasing temperature, while the singlet state emission at 415 nm exhibits resistance to thermal quenching. Additionally, both singlet and triplet emissions exhibit a red-shift with increasing temperature, indicating a temperature-induced change in the electronic structure of the material.[15,31] The CIE coordinates, presented in Fig. 3b, illustrate the color change of *R*-CCCH:Sn^{2+} from yellow (0.3132, 0.4036) to pink-violet (0.2681, 0.2621) and eventually to cyan (0.2083, 0.2023) as the temperature increases. This color change is consistent with the optical images shown in Fig. 3c, where the emission color shifts from yellow to cyan under UV light exposure at different temperatures. The final cyan emission was similar to the luminescence color of *P*-CCCH:Sn^{2+} under UV light.

In contrast, the temperature-dependent PL spectra of *P*-CCCH:Sn^{2+}, depicted in Fig. 3d, show a significant decrease in the emission peak at 492 nm with a blueshift as the temperature increases. This blueshift may be attributed to structural distortions in the crystal lattice at high temperatures. The corresponding CIE coordinates, shown in Fig. 3e, indicate a color transition from cyan (0.1829, 0.2988) to blue (0.1712, 0.2022) for *P*-CCCH:Sn^{2+} as the temperature rises from 298 K to 428 K, which is in agreement with the optical images shown in Fig. 3f. These observations suggest that the non-luminescent *R*-CCCH material is metastable and transforms into stable, blue-emitting *P*-CCCH upon heating, a process that is irreversible. It is also noted that Sn^{2+} ions emit both singlet and triplet states in *R*-CCCH, while only triplet emission is observed in *P*-CCCH.

Fig. S7† shows the temperature-dependent emission spectra of *R*-CCCH:Sn^{2+} from 77 K to 298 K, exhibiting the same phenomena observed at higher temperatures. In Fig. S8,† the Huang–Rhys factors for the *R*-CCCH:Sn^{2+} sample were calculated to be 30.9 (singlet state) and 21.3 (triplet state), indicating strong electron–phonon coupling for both emission

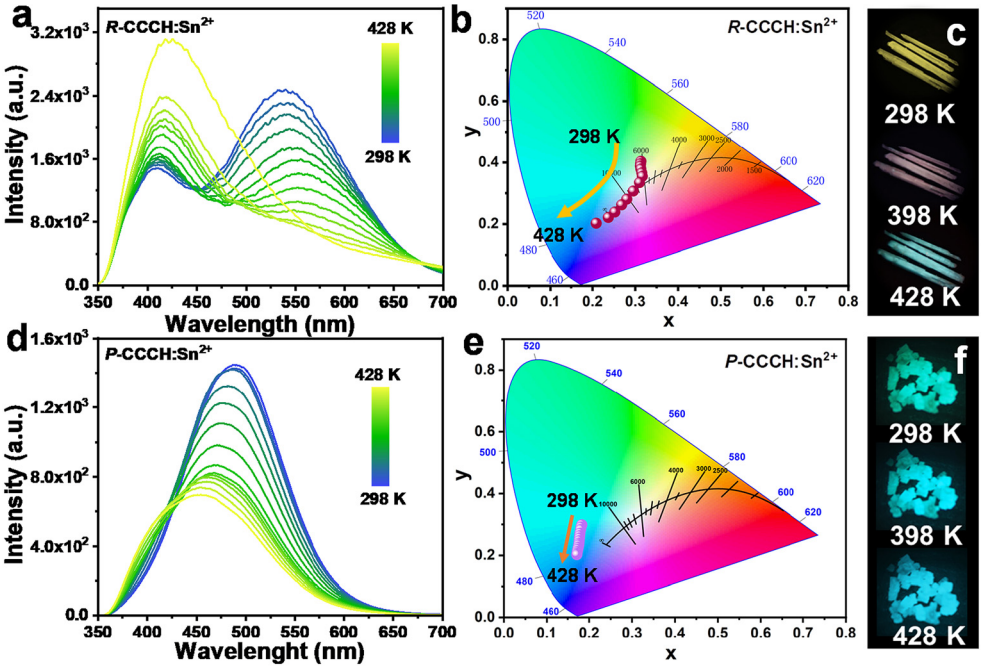

Fig. 3 PL spectra, CIE coordinates and optical photographs of (a–c) *R*-CCCH:Sn^{2+} and (d–f) *P*-CCCH:Sn^{2+} excited at 284 nm wavelength in the range of 298–428 K.

peaks.[23,32,33] These results provide valuable insights into the luminescence behavior and stability of Sn^{2+} doped CCCH materials, which are essential for their potential applications in optoelectronic devices operating under varying temperature conditions.

The sample labeled as *R*-CCCH:Sn^{2+} after calcination (*R*-CCCH:Sn^{2+}-AC) was subjected to calcination at 428 K for 20 minutes. Under UV light irradiation, the emission color of *R*-CCCH:Sn^{2+}-AC transformed from yellow to cyan post-calcination, and this cyan emission persisted even after cooling, aligning with the luminescence color of *P*-CCCH:Sn^{2+} material. To investigate the intrinsic correlation between the calcined *R*-CCCH:Sn^{2+}-AC and *P*-CCCH:Sn^{2+} samples, XRD, photoluminescence (PL) spectra, and PL lifetimes were determined. Fig. 4a reveals that the XRD pattern of *R*-CCCH:Sn^{2+}-AC matches well with the standard card, with only changes in the intensity of diffraction peaks, indicating no alteration in the crystal structure of the material. Simultaneously, the XRD diffraction peaks of *P*-CCCH:Sn^{2+} in Fig. 4b are in good agreement with the standard card, and the relative intensities of the *P*-CCCH:Sn^{2+} diffraction peaks are essentially consistent. It is preliminarily concluded that *R*-CCCH:Sn^{2+} is in a metastable state and transitions to the more stable *P*-CCCH:Sn^{2+} under heating conditions.

To further ascertain the relationship between the two, a comparative analysis of the emission spectra of *R*-CCCH:Sn^{2+}-AC and *P*-CCCH:Sn^{2+} was performed (Fig. 4c). The emission peaks consist of two components: the blue region attributed to the STEs of CCCH matrix and the pink region corresponding to the $^3P_1 \rightarrow {}^1S_0$ transition of Sn^{2+}. The PL lifetime curves in

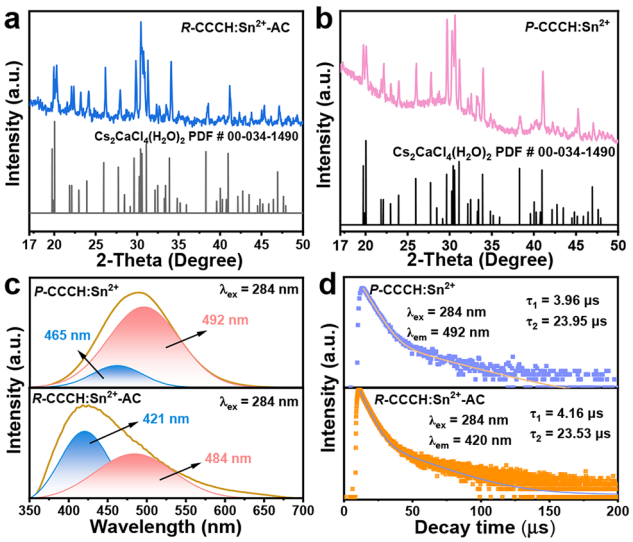

Fig. 4 Powder XRD patterns of (a) *R*-CCCH:Sn^{2+} and (b) *P*-CCCH:Sn^{2+} after calcination (*R*-CCCH:Sn^{2+}-AC) at 428 K. (c) PL spectra and (d) PL lifetimes of *R*-CCCH:Sn^{2+}-AC and *P*-CCCH:Sn^{2+}.

Fig. 4d indicate that the lifetimes of *R*-CCCH:Sn^{2+}-AC (τ_1 = 4.16 μs, τ_2 = 25.35 μs) are consistent with those of the *P*-CCCH:Sn^{2+} crystal (τ_1 = 3.96 μs, τ_2 = 23.95 μs), further suggesting that the luminescence mechanism of the calcined *R*-CCCH:Sn^{2+}-AC sample is identical to that of the *P*-CCCH:Sn^{2+} crystal. Therefore, it is further confirmed that *R*-CCCH:Sn^{2+} is in a metastable state, while *P*-CCCH:Sn^{2+} is in a stable state. These

findings provide a deeper understanding of the phase transformation and luminescence properties of Sn^{2+} doped CCCH materials under thermal treatment, which is crucial for their potential applications in optoelectronic devices.

The construction of a warm white light-emitting diode (WLED) utilizing *R*-CCCH:Sn^{2+} and the commercial red phosphor K_2SiF_6:Mn^{4+} co-packaged on a 285 nm ultraviolet chip is detailed in Fig. 5a. The electroluminescence (EL) spectra exhibit peaks at 415 nm and 540 nm, corresponding to the singlet and triplet emissions of Sn^{2+} in *R*-CCCH, respectively. Additionally, the narrow-band red emission at 640 nm is attributed to the characteristic emission of the commercial red phosphor K_2SiF_6:Mn^{4+}. As depicted in Fig. 5b, the CIE color coordinates of the WLED are (0.3624, 0.4009), with a corresponding color temperature of 4636 K and a high color rendering index (CRI) of 92. These values indicate that the WLED provides a balanced and natural white light, suitable for various lighting applications.

Furthermore, to explore the potential of *R*-CCCH:Sn^{2+} for temperature-sensitive anti-counterfeiting applications, leaf patterns were engraved on a 3 × 3 cm glass substrate using laser carving, which was then coated with the *R*-CCCH:Sn^{2+} sample layer. Fig. 5c illustrates the changes in the luminescence color of the leaf pattern under UV irradiation as the temperature varies. At 298 K, a bright yellow emission is observed. As the temperature increases from room temperature to 428 K, the luminescence of the *R*-CCCH:Sn^{2+} sample transitions from yellow to pink-purple and finally to cyan. This color transformation demonstrates the temperature-sensitive luminescence properties of *R*-CCCH:Sn^{2+}, suggesting its utility in anti-counterfeiting technologies that require temperature-based authentication.

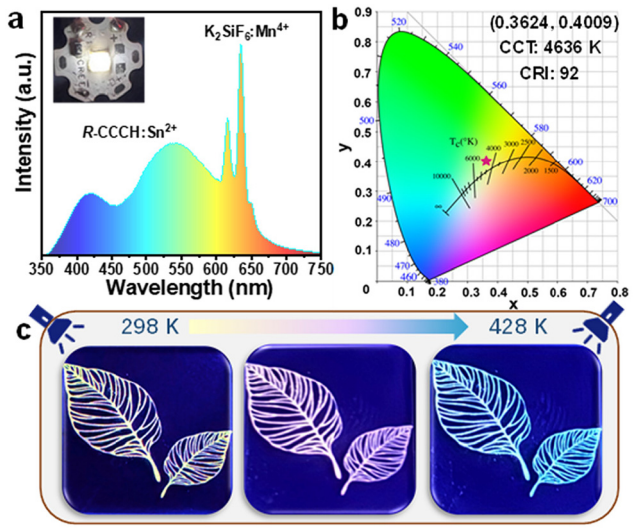

Fig. 5 (a) Electroluminescence spectra of WLED constructed using the *R*-CCCH:Sn^{2+} and red commercial phosphor K_2SiF_6:Mn^{4+} on a 285 nm ultraviolet chip under 30 mA current (inset: image of the WLED device in the working state). (b) CIE color coordinates of WLED. (c) Designed leaf patterns for temperature-sensitive anti-counterfeiting application under UV irradiation.

4 Conclusions

In conclusion, our research has successfully demonstrated the synthesis of rod-like *R*-CCCH *via* hydrothermal methods, showcasing its unique luminescence properties upon doping with Sn^{2+} ions. The study highlights the dual-state white light emission arising from the simultaneous transitions of Sn^{2+} ions, with distinct emissions at 415 nm and 540 nm. The metastable *R*-CCCH:Sn^{2+} not only possesses remarkable luminescence properties but also offers a promising route for the development of temperature sensing devices and anti-counterfeiting technologies due to the transformation to a stable state *P*-CCCH:Sn^{2+} upon heating. This work contributes to the broader understanding of Sn^{2+} doped luminescent materials, highlighting the significance of metastable states of the host lattice in enhancing their functional performance.

Data availability

The data supporting the findings of this study are openly available upon request from the corresponding author, Yuexiao Pan, at yxpan@wzu.edu.cn. Data will be shared promptly, subject to no privacy or proprietary restrictions.

For access to the data, interested parties should submit a brief request outlining the specific data needed and their research purpose. The authors will review and respond to requests within a reasonable timeframe.

For any inquiries regarding data availability, please contact the corresponding author.

Conflicts of interest

There are no conflicts to declare.

Acknowledgements

This research is financially supported by the Key R&D Program of Zhejiang Province (Grant No. 2024C01193), the National Natural Science Foundation of China (52172152 and 52172166), the Seedling Program Project of Zhejiang Province (2024R429A013), and the Graduate Student Innovation Foundation of Wenzhou University (3162024001001 and 3162024003043).

References

1 T. H. Chen, Y. J. Ma and D. P. Yan, Single-Component 0D Metal–Organic Halides with Color-Variable Long-Afterglow

toward Multi-Level Information Security and White-Light LED, *Adv. Funct. Mater.*, 2023, **33**, 2214962.

2 S. D. Adhikari, S. K. Dutta, A. Dutta, A. K. Guria and N. Pradhan, Chemically Tailoring The Dopant Emission in Manganese-Doped $CsPbCl_3$ Perovskite Nanocrystals, *Angew. Chem., Int. Ed.*, 2017, **56**, 8746–8750.

3 S. G. Zhou, Y. H. Chen, K. L. Li, X. W. Liu, T. Zhang, W. Shen, M. Li, L. Zhou and R. X. He, Photophysical Studies for Cu(I)-Based Halides: Broad Excitation Bands and Highly Efficient Single Component Warm White-Light-Emitting Diodes, *Chem. Sci.*, 2023, **14**, 5415–5424.

4 B. Zhou, A. X. Du, D. Ding, Z. X. Liu, Y. Wang, H. Z. Zhong, H. A. Li, H. L. Hu and Y. M. Shi, Achieving Tunable Cold/Warm White-Light Emission in a Single Perovskite Material with Near-Unity Photoluminescence Quantum Yield, *Nano-Micro Lett.*, 2023, **15**, 207.

5 Z. Z. Zhang, J. C. Jin, Y. P. Lin, H. P. Xu, J. Cheng, H. M. Zeng, Z. E. Lin, Z. G. Xia and G. H. Zou, Multisite Fine-Tuning in Hybrid Cadmium Halides Enables Wide Range Emissions for Anti-Counterfeiting, *Angew. Chem., Int. Ed.*, 2024, **63**, e202400760.

6 C. H. Wei, S. P. Dong, Z. H. Xu, M. Z. Li, T. Zhang, Z. B. Xu, S. Lan, S. Wang and L. Mao, Controllable Multi-exciton Zero-Dimensional Antimony-based Metal Halides for White-Light Emission and β-Ray Detection, *Angew. Chem., Int. Ed.*, 2024, **63**, e202412253.

7 L. K. Wu, R. F. Li, W. Y. Wen, Q. H. Zou, H. Y. Ye and J. R. Li, Lead-Free Hybrid Indium Perovskites with Near unity PLQY and White Light Emission Using an Sb^{3+} Doping Strategy, *Inorg. Chem. Front.*, 2023, **10**, 3297–3306.

8 H. X. Yang, X. X. Chen, H. L. Lu, Y. Li, W. D. Sun, Y. H. Zhang, X. W. Liu, G. K. Long, L. B. Zhang and X. Y. Li, Self-Trapped Excitons-Based Warm-White Afterglow by Room-Temperature Engineering toward Intelligent Multi-Channel Information System, *Adv. Funct. Mater.*, 2024, **34**, 2311437.

9 J. J. Wu, X. L. Li, X. Lian, B. B. Su, J. H. Pang, M. D. Li, Z. G. Xia, J. Z. Zhang, B. B. Luo and X. C. Huang, Ultrafast Study of Exciton Transfer in Sb(III)-Doped Two-Dimensional $[NH_3(CH_2)_4NH_3]CdBr_4$ Perovskite, *ACS Nano*, 2021, **15**, 15354–15361.

10 D. A. Popy, B. N. Evans, J. Jiang, T. D. Creason, D. Banerjee, L. M. Loftus, R. Pachter, D. T. Glatzhofer and B. Saparov, Intermolecular Arrangement Facilitated Broadband Blue Emission in Group-12 Metal (Zn, Cd) Hybrid Halides and Their Applications, *Mater. Today Chem.*, 2023, **30**, 101502.

11 J. H. Yuan, T. C. Wang, Y. Zhang, S. Y. Yao, L. L. Han, D. D. Mu, H. Song, J. Y. He, F. Zhang and X. Xu, A Zero-Dimensional Perovskite with High-Effficiency Luminescence and Transient Response for Advanced Information Encryption, *Chem. Eng. J.*, 2024, **496**, 153939.

12 W. Liao, X. Q. Zhou, J. C. Jin, Y. Z. Wang and Z. G. Xia, Screening Thermochromic Luminescent Materials in Cs-Cd-Br Ternary Phase Diagram for Temperature Visualization Applications, *Laser Photonics Rev.*, 2024, **18**, 2400194.

13 C. L. Zhao, Y. Gao and J. B. Qiu, Achieving Multicolor Emitting of Antimony-Doped Indium-Based Halide Perovskite via Monovalent Metal Induced Phase Engineering, *ACS Appl. Mater. Interfaces*, 2023, **15**, 59610–59617.

14 Y. Liu, S. P. Yan, T. C. Wang, Q. S. He, X. D. Zhu, C. Wang, D. Y. Liu, T. Wang, X. H. Xu and X. Yu, Achieving Color-Tunable Long Persistent Luminescence in Cs_2CdCl_4 Ruddlesden-Popper Phase Perovskites, *Angew. Chem., Int. Ed.*, 2023, **62**, e202308420.

15 J. D. Yao, H. Y. Wang, J. Wu, B. S. Zou and R. S. Zeng, Boosting Photoluminescence of Rare-Earth-Based Double Perovskites by Isoelectronic Doping of ns^2 Metal Ions, *Small*, 2024, 2405724.

16 F. M. Zhu, Y. Gao and J. B. Qiu, High Performance NIR-I to NIR-II Emission of a Cr^{3+}-doped $Cs_2NaLuCl_6$ Phosphor with an IQE and EQE of Up to 92.9% and 60.75%, *Inorg. Chem. Front.*, 2024, **11**, 7098–7109.

17 J. C. Jin, Y. Z. Wang, K. Han and Z. G. Xia, Rigid Phase Formation and Sb^{3+} Doping of Tin(IV) Halide Hybrids toward Photoluminescence Enhancement and Tuning for Anti-Counterfeiting and Information Encryption, *Angew. Chem., Int. Ed.*, 2024, **63**, e202408653.

18 X. Y. Wang, Q. B. Shen, Y. S. Chen, N. Ali, Z. Y. Ren, G. Bi and H. Z. Wu, Self-Trapped Exciton Emission in an Sn(II)-doped All-Inorganic Zero-Dimensional Zinc Halide Perovskite Variant, *Nanoscale*, 2021, **13**, 15285–15291.

19 G. Y. Zhang, D. Y. Wang, J. J. Ren, X. P. Zhou and Y. H. Wang, Highly Efficient Broadband Near-Infrared Emission from Sn^{2+} Alloyed Lead-Free Cesium Zinc Halides, *Laser Photonics Rev.*, 2023, **17**, 2300158.

20 T. H. Chen and D. P. Yan, Full-Color, Time-Valve Controllable and Janus-Type Long-Persistent Luminescence from All-Inorganic Halide Perovskites, *Nat. Commun.*, 2024, **15**, 5281.

21 J. L. Yao, C. Cao, H. M. Cheng, D. Y. Wang, W. S. Yang and R. G. Xie, All-Inorganic Zero-Dimensional Sn-Doped Rb_4CdCl_6 with Near-Unity Quantum Efficiency, *J. Phys. Chem. C*, 2023, **127**, 3602–3608.

22 H. Wang, Y. X. Pan, Y. H. Ding, H. Z. Lian, J. Lin and L. Y. Li, Tunable Multicolor Emission and High Thermal Stability in Single-Matrix Luminescent Crystals Based on Calcium Perovskites for Advanced Solid-State Lighting Applications, *Adv. Opt. Mater.*, 2024, **12**, 2400935.

23 L. W. Zhang, H. Zhou, Y. B. Chen, Z. M. Zheng, L. S. Huang, C. Wang, K. L. Dong, Z. Q. Hu, W. J. Ke and G. J. Fang, Spontaneous Crystallization of Strongly Confined $CsSn_xPb_{1-x}I_3$ Perovskite Colloidal Quantum Dots at Room Temperature, *Nat. Commun.*, 2024, **15**, 1609.

24 X. Chen, Z. H. Lu, Y. X. Pan, Y. H. Ding, H. Z. Lian, J. Lin and L. Y. Li, Tunable Spectral Emission from 0D Rb_3ZnBr_5 Crystals for Single-Component Multi-Color LED Applications, *Laser Photonics Rev.*, 2024, 2401061.

25 Y. H. Zhang, B. J. Chen, X. Z. Zhang, Y. Z. Cao, J. S. Zhang, S. Xu, X. P. Li, H. Q. Yu, D. Gao, X. Z. Sha, L. Wang, X. Chen and H. Lin, Sn^{2+}/Mn^{2+} Co-Doped Germanate Glass

with Quasi-Sunlight Spectrum Visible-Emission and Its High-Quality W-LED Application, *Chem. Eng. J.*, 2023, **467**, 143467.

26 J. F. Liao, Z. P. Zhang, L. Zhou, Z. K. Tang and G. C. Xing, Achieving Near-Unity Red Light Photoluminescence in Antimony Halide Crystals via Polyhedron Regulation, *Angew. Chem., Int. Ed.*, 2024, **63**, e202404100.

27 H. B. Sun, X. Y. Yang, P. L. Li, Y. F. Bai, Q. C. Meng, H. Y. Zhao, Q. J. Wang, Z. Y. Wen, L. Huang, D. Huang, W. W. Yu, H. B. Chen and F. Liu, Solution Synthesis and Light-Emitting Applications of One-Dimensional Lead-Free Cerium(III) Metal Halides, *Nano Lett.*, 2024, **24**, 10355–10361.

28 F. Zhang, X. Chen, X. Qi, W. Liang, M. Wang, Z. Ma, X. Ji, D. Yang, M. Jia, D. Wu, X. Li, Y. Zhang, Z. Shi and C. Shan, Regulating the Singlet and Triplet Emission of Sb^{3+} Ions to Achieve Single-Component White-Light Emitter with Record High Color-Rendering Index and Stability, *Nano Lett.*, 2022, **22**, 5046–5054.

29 S. Y. Yu, H. Peng, Q. L. Wei, T. Z. Li, W. G. Huang, X. F. He, Z. T. Du, J. L. Zhao and B. S. Zou, Realizing Efficient Broadband Near-Infrared Emission and Multimode Photoluminescence Switching via Coordination Structure Modulation in Sb^{3+} -Doped 0D Organic Metal Chlorides, *Mater. Horiz.*, 2024, **11**, 2230–2241.

30 F. Jiang, Z. N. Wu, M. Lu, Y. B. Gao, X. Li, X. Bai, Y. Ji and Y. Zhang, Broadband Emission Origin in Metal Halide Perovskites: Are Self-Trapped Excitons or Ions?, *Adv. Mater.*, 2023, **35**, 2211088.

31 S. Kumar, R. S. Lamba, S. Monga, V. Jha, S. Saha, S. Bhattacharya and S. Sapra, Broad Dual Emission from $Cs_2Zr_{1-x}Mo_xCl_6$: Enhancing the NIR Emission in Lead-Free Vacancy Ordered Double Perovskites, *Chem. Mater.*, 2024, **36**, 4561–4570.

32 R. Jiang, G. Q. Peng, Q. J. Li, H. X. Wang, Z. P. Ci and Q. Wang, Manganese(II) Halides for X-Ray Imaging and Moisture Detection, *Adv. Mater. Technol.*, 2024, **9**, 2301894.

33 B. Lian, H. W. Hou, F. P. Lin, B. B. Luo, D. C. Pan, B. S. Zou and R. S. Zeng, Multimode Luminescence with Temperature and Energy Level Synergistic Dependence in Rare Earth Halide DPs for Advanced Multifunctional Applications, *Small*, 2024, **20**, 2401093.

